ACS APPLIED MATERIALS & INTERFACES

Research Article

www.acsami.org

Enhanced Activity for CO Oxidation over WO_3 Nanolamella Supported Pt Catalyst

Jiajun Wang, Zongyuan Wang, and Chang-Jun Liu*

Collaborative Innovation Center of Chemical Science and Engineering, School of Chemical Engineering and Technology, Tianjin University, Tianjin 300072, China

Supporting Information

ABSTRACT: WO_3 nanolamella supported Pt catalyst has been prepared and applied for CO oxidation in this work. A significantly enhanced activity has been achieved, compared to that of the Pt catalyst supported by the WO_3 nanoparticle. The catalyst characterization using X-ray diffraction (XRD), scanning electronic microscopy (SEM), high-resolution transmission electron microscopy (HRTEM), and N_2 adsorption−desorption confirms that the WO_3 nanolamella supported Pt catalyst possesses higher Pt dispersion, improved metal−support interaction with a higher electron density of Pt, and a weak adsorption of CO, leading to the significantly enhanced activity for CO oxidation.

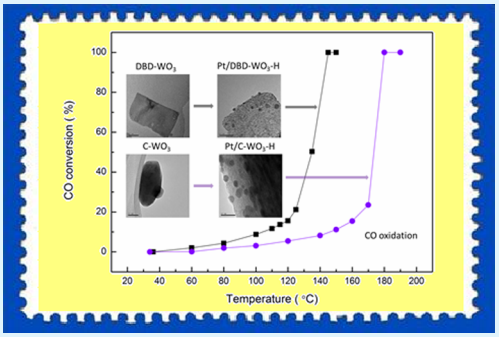

KEYWORDS: *WO_3, morphology, catalyst, platinum, CO oxidation*

1. INTRODUCTION

Catalyst plays a very important role in chemical synthesis. The use of catalyst has become one of 12 principals of green chemistry.[1] With the development of clean fuel, renewable energy, shale gas conversion, biogas utilization, and many others, catalyst will find much more important applications in the future. One popular topic in catalytic investigations is the effect of the morphology of the catalyst or the supporting material on the properties of the catalyst, such as metal−support interaction, adsorption, and reactivity.[2−13] One can easily find many articles on this topic in the literature. In this work, we attempt to study the morphological effect of WO_3 as supporting material on the activity of Pt catalyst for CO oxidation. It is well-known that Pt on various supporting materials shows good activities for CO oxidation. The supporting materials investigated include inert oxides, such as Al_2O_3 and SiO_2, and reducible oxides, including Fe_2O_3, TiO_2, Co_3O_4, CeO_2, and so on.[14−17] The reducible oxide supported catalysts usually exhibit activities higher than those of the inert oxide supported catalysts with the same Pt loading. The enhanced activities are principally from weak adsorption of CO and better supplement of active oxygen species. However, few studies on CO oxidation on WO_3 have been performed. We chose WO_3 not only because it is a reducible oxide but also because it presents in several different morphologies with different properties for sensors, catalysts, and electrochromic displays.[18−23] WO_3 is an important oxide with various nanostructures including nanorods, nanoflakes, and nanolamellas.[18,20,21] It is a very promising oxide for the catalytic applications. To the best of our knowledge, there is still no reported study on the morphological effect of WO_3 on the activity for CO oxidation. In this work, we attempt to compare the activities of WO_3 nanolamella supported Pt and WO_3 nanoparticle supported Pt catalysts for CO oxidation. A conventional impregnation was employed to synthesize Pt catalysts supported on WO_3 materials. We confirm that the WO_3 nanolamella supported Pt catalyst shows higher Pt dispersion, enhanced metal−support interaction, and higher catalytic activity for CO oxidation. We use a new way here to fabricate WO_3 nanolamella by using dielectric-barrier discharge (DBD) plasma decomposition at low temperature with neither template nor thermal calcination. DBD is a conventional cold plasma phenomenon that has been applied for the industrial production of ozone, plasma TV, and others. The DBD plasma decomposition of catalyst precursors have been previously applied for the production of zeolite and other catalysts at atmospheric pressure and temperatures lower than 200 °C.[24−29] The DBD-made WO_3 nanolamella shows higher BET surface area than that of WO_3 nanoparticle synthesized by thermal calcination.

2. EXPERIMENTAL SECTION

2.1. Preparation of the Catalysts. WO_3 used in this work was synthesized by the decomposition of tungstic acid. Tungstic acid was prepared in this way: 50 mL of a solution of Na_2WO_4 (1 M; >99.5%; Kemiou Company, Tianjin, China) was added dropwise to 450 mL of an aqueous solution of HCl (3 M; 36% ∼ 38%; made in Jiangtian Chemical Plant, Tianjin, China), and the mixture was stirred. A yellow precipitate was obtained. After the sample was aged for 1 h, the

Received: May 8, 2014
Accepted: June 26, 2014
Published: June 26, 2014

precipitate was filtered, washed with distilled water several times, and dried at 100 °C for 12 h in a drying oven. The dried sample ($WO_3 \cdot nH_2O$) was then divided into two parts. One part was thermally calcined at 600 °C for 2 h. The product was denoted as C-WO_3. The other part was decomposed under DBD plasma to make WO_3 nanolamella. The DBD plasma decomposition has been previously described in detail.[24−29] Briefly, two steel plate electrodes were attached to two quartz plates (the dielectric materials) with a thickness of 2 mm. The diameters of the quartz plates and the steel plates are 90 and 50 mm, respectively. The width of the discharge gap (i.e., the distance between the two quartz plates) is 8 mm. The $WO_3 \cdot nH_2O$ powder (0.7 g) was placed on the lower quartz plate. Air was directly used as the plasma forming gas. A high voltage generator (CTP-2000 K; Corona Laboratory, Nanjing, China), which can supply a voltage from 0 to 30 kV with a sinusoidal waveform at a frequency of about 22 kHz, was used to generate the DBD plasma. The average voltage used during the decomposition was 14 kV. Each DBD decomposition operation was performed for 3 min and was repeated 25 times. After each operation, the sample was manually stirred. The final product, WO_3 nanolamella, was denoted as DBD-WO_3.

The Pt/WO_3 catalysts containing 2.5 wt % Pt were prepared by the incipient wetness impregnation method. In a typical synthesis procedure, an aqueous solution of H_2PCl_6 (2 mL; 0.1 M; Delan, Tianjin, China) was added to 0.573 g of DBD-WO_3 support, and the mixture was stirred continuously for 1 h and allowed to stand for 12 h. The sample was then dried at 110 °C for 12 h. The obtained catalyst was denoted as Pt/DBD-WO_3. The catalyst with the C-WO_3 support was prepared in a similar way and was denoted as Pt/C-WO_3.

2.2. Catalyst Characterization. X-ray diffraction (XRD) patterns were recorded on a Rigaku D/MAX-2500 V/PC diffractometer with a Cu Kα radiation source (λ = 0.154056 nm). The X-ray source was operated at 40 kV and 200 mA. The wide-angle XRD patterns were collected at a scanning speed of 4°/min over the 2θ range from 5° to 90°. Phase identification of the samples was made by comparison to the Joint Committee on Powder Diffraction Standards (JCPDSs).

Scanning electronic microscopy (SEM) study was performed on an FEI NanoSEM 430.

High-resolution transmission electron microscopy (HRTEM) measurements were carried out on a Philips Tecnai G2F20 system operated at 200 kV. Before the measurement was performed, the samples were suspended in ethanol with ultrasonic dispersion for 60 min. Then the resulting suspension was dropped on a copper grid coated with carbon. The particle size distribution of Pt was measured from the TEM images with more than 120 particles.

N_2 adsorption−desorption isotherms were recorded using a Micromeritics TriStar 3000 instrument. The samples were degassed under vacuum at 200 °C for 6 h. The specific surface areas of the samples were calculated with the Brunauer−Emmett−Teller (BET) equation (relative pressure from 0.1 to 0.3).

X-ray photoelectron spectroscopy (XPS) analyses were performed on a Perkin-Elmer PHI-1600 spectrometer with monochromatic Mg Kα (1253.6 eV) radiation. Binding energies were calibrated using the C 1s peak (284.6 eV) as a reference.

Hydrogen temperature-programmed reduction (H_2-TPR) was conducted on a TPDRO 1100 apparatus (Thermo Finnigan, LLC). A gaseous mixture of 5 vol % H_2 in N_2 was used as reductant at a flow rate of 20 mL/min. Before detection by a thermal conductivity detector (TCD), the gas was purified by a trap containing CaO + NaOH materials to remove H_2O and CO_2. Approximately 100 mg of the sample was heated from room temperature to 900 °C at a rate of 10 °C/min.

CO-adsorbed diffuse reflectance infrared Fourier transform (DRIFT) spectra were recorded on a Tensor 27 spectrometer (Bruker) with a resolution of 4 cm^{-1} and 64 scans. The apparatus was equipped with a liquid nitrogen cooled mercury−cadmium−tellurium (MCT) detector, a diffuse reflectance accessory, and a high-temperature reaction chamber (Praying Mantis, Harrick). Before the measurement, the samples were reduced in 30 mL/min H_2 at 300 °C for 2 h and purged by flowing helium (30 mL/min) at 300 °C for 30 min to remove water and gas residue. CO adsorption was carried out in 20 mL/min CO (1.11 vol %)/argon for 30 min at 25 °C. All spectra were illustrated using Kubelka−Munk units, which are linear with the concentration of surface species.

2.3. CO Oxidation. CO oxidation was performed in a quartz tube (i.d. 4 mm) under atmospheric pressure. The WO_3 supported Pt catalyst was packed into the tube. Before the reaction, the sample was heated to 300 °C (10 °C/min) in 30 mL/min argon and kept for 30 min. Then the sample was reduced in 30 mL/min H_2 at 300 °C for 2 h and cooled to 30 °C in argon. Subsequently, CO oxidation was initiated in a flowing mixture of CO, O_2, and N_2 (20 mL/min; 1.0 vol % CO, 20.0 vol % O_2, balance N_2). The effluent was then analyzed online by a gas chromatograph (Agilent 6890) equipped with a 2-m TDX-01 packed column and a thermal conductivity detector (TCD) using argon as the carrier gas.

3. RESULTS AND DISCUSSION

3.1. Characterization of WO_3 Materials. *3.1.1. XRD Characterization.* Figure 1 shows the XRD patterns of DBD-

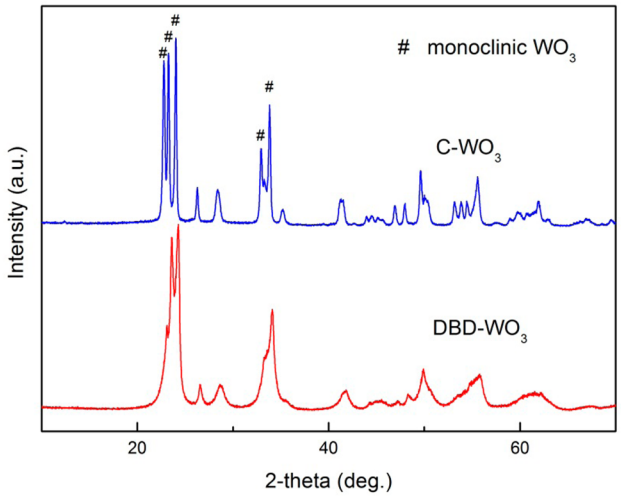

Figure 1. XRD patterns of DBD-WO_3 and C-WO_3.

WO_3 and C-WO_3. The diffraction peaks at 23.1°, 23.6°, 24.4°, and 34.2° are attributed to the (002), (020), (200), and (202) lattice planes of the monoclinic structure of WO_3 with a = 7.297 Å, b = 7.539 Å, c = 7.6988 Å, and β = 90.91°, respectively (JCPDS card no. 43-1035). Both samples are in pure phase, and peaks of other impurities are not detected. The peaks of C-WO_3 are more intense, compared with those of DBD-WO_3, indicating that C-WO_3 has higher crystallinity than DBD-WO_3. The mean nanoparticle size of DBD-WO_3 is 13.0 nm, while it is 32.8 nm for C-WO_3, calculated using Scherrer equation (using WO_3 (020)). This indicates that DBD decomposition generates smaller particles. It is worth noting that the intensity of (002) peak of C-WO_3 is much higher than that of DBD-WO_3, indicating an inhibition of the growth of (002) plane on DBD-WO_3, which affects the morphology of the samples.

3.1.2. SEM and TEM Analyses. Figure 2 shows SEM images of DBD-WO_3 and C-WO_3. It reveals the lamellar-like particles with DBD-WO_3, while the C-WO_3 sample consists of irregular particles in larger sizes. The thickness and size of the samples measured by the SEM images are summarized in Table 1.

Figure 3 shows TEM images of DBD-WO_3 and C-WO_3. The formation of rectangle-like nanolamella with a lateral size around 30−80 nm is observed in Figure 3a. Meanwhile, some rough surfaces with spots are observed over DBD-WO_3. The apparent differences between the samples confirm the effect of

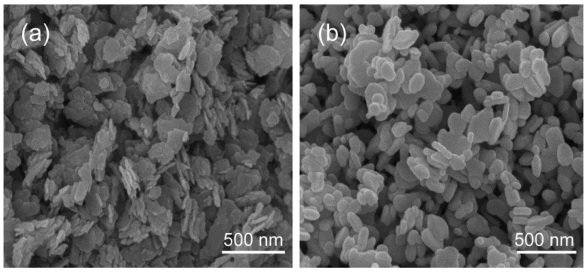

Figure 2. SEM images of (a) DBD-WO_3 and (b) C-WO_3.

preparation conditions on the catalyst morphology. The lattice fringes with d = 0.376 and 0.366 nm, corresponding to the (020) and (200) planes of monoclinic WO_3, are observed in the two samples (shown in Figure 3c,d). Meanwhile, (002) planes are not observed in DBD-WO_3. However, compact lattice fringes (d = 0.266 nm) are observed in Figure 3d. The differences in the corresponding SAED patterns of the samples show additional lattice planes of C-WO_3((002) and ($\bar{2}$02) planes). Xie et al. reported that the surface energies follow an order of (002) > (020) > (200), indicating that the (002) plane is the most unstable.[30] Kida et al. reported a formation of WO_3 nanolamella after calcination at 300 °C, which is similar to our results.[18] Therefore, it is inferred that DBD decomposition might lead to a rapid growth along [010] and [100] directions and inhibit the growth along [001] direction, while calcination at 600 °C simultaneously promotes the growth of [010], [100], [001], and other orientations, leading to the different morphologies of the samples.

3.1.3. N_2 Adsorption–Desorption. The nitrogen adsorption–desorption isotherms of DBD-WO_3 and C-WO_3 are shown in Figure 4. Different from that of C-WO_3, the isotherm of DBD-WO_3 shows a hysteresis loop, indicating that the material might contain some mesopores. Table 1 shows the textural properties of the samples. The specific surface area of DBD-WO_3 (40.7 m^2/g) is significantly higher than that of C-WO_3 (12.5 m^2/g). Pore size distributions were calculated using the Barrett–Joyner–Halenda (BJH) formula. DBD-WO_3 exhibits two peaks at 2.2 and 30.0 nm, while C-WO_3 shows irregular pore size distribution. However, from Figures 2 and 3, no clear pores or channels are observed in a single particle. Therefore, the pore size distribution might be caused by the irregular stacking of the particles.

3.2. Characterization of Pt/WO_3 Catalysts and Their Catalytic Activities for CO Oxidation. *3.2.1. CO Oxidation.* CO conversions as a function of temperatures for Pt/DBD-WO_3, Pt/C-WO_3, DBD-WO_3, and C-WO_3 are shown in Figure 5. CO conversion of Pt/DBD-WO_3 and Pt/C-WO_3 increases with increasing temperature. Pt/DBD-WO_3 exhibits higher activity compared with Pt/C-WO_3. Pure DBD-WO_3 and C-WO_3 show no activity within the temperature range tested. Pt/DBD-WO_3 and Pt/C-WO_3 show typical light-off temperatures (20% conversion) at 120 and 150 °C, respectively. The corresponding temperatures with 100% CO conversion are 145

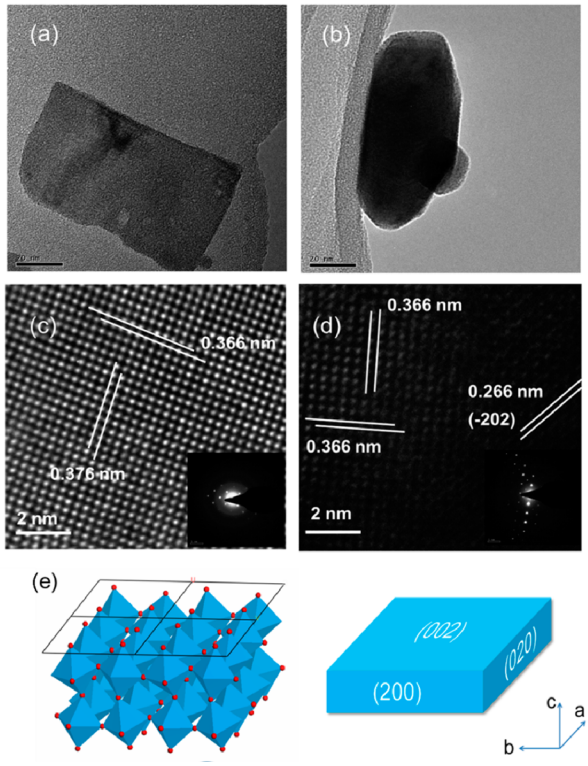

Figure 3. TEM images of (a) WO_3 nanolamella and (b) WO_3 nanoparticle after ultrasonic dispersion in ethanol; HRTEM images of (c) DBD-WO_3 and (d) C-WO_3 (corresponding SAED patterns are displayed in the insets); and (e, left) atomic structure model of (002) facet and (right) model of WO_3 nanolamella.

and 180 °C, respectively. Turnover frequencies (TOF) based on Pt dispersion were calculated at three temperatures (80, 100, and 120 °C). The TOF values of the samples are shown in Figure 6. The dispersion is estimated from the mean particle diameters obtained from TEM analyses. The TOFs of the catalysts also increase with increasing temperature. From Figures 5 and 6, Pt/DBD-WO_3 shows a significantly enhanced catalytic activity for CO oxidation. Compared with Pt/C-WO_3, Pt/DBD-WO_3 dramatically reduces the light-off temperature and T_{100} (100% CO conversion). Within the range of reaction temperatures, all the catalysts exhibit an excellent stability with time. An example of the stability test is shown in Figure S5 (Supporting Information).

3.2.2. XRD Characterization. The XRD patterns of Pt/DBD-WO_3 and Pt/C-WO_3 after reduction in H_2 (denoted as Pt/DBD-WO_3–H and Pt/C-WO_3–H) are shown in Figure 7. The diffraction peaks at 39.8° and 46.2° are assigned to Pt (111) and (200), respectively (JCPDS card no. 65-2868). When we compare the two patterns, we see that the intensity of the Pt reflection peaks of Pt/DBD-WO_3–H decrease, suggesting a smaller particle size and a higher dispersion over Pt/DBD-WO_3–H. The patterns of tungsten oxide in Figures 1 and 7 change significantly after H_2 reduction. The peaks of

Table 1. Crystallite Sizes, Lateral Sizes, Thicknesses, and Specific Surface Areas of DBD-WO_3 and C-WO_3

sample	crystallite size (nm)[a]	thickness (nm)[b]	lateral size (nm)[b]	specific surface area (m^2/g)	pore size (nm)
DBD-WO_3	13.0	18.6–27.8	56.1–96.8	40.7	2.2, 30.0
C-WO_3	32.8		75.8–150.6	12.5	

[a]Crystallite size was calculated using XRD peak of the (020) plane. [b]Thickness and lateral size were estimated from SEM images.

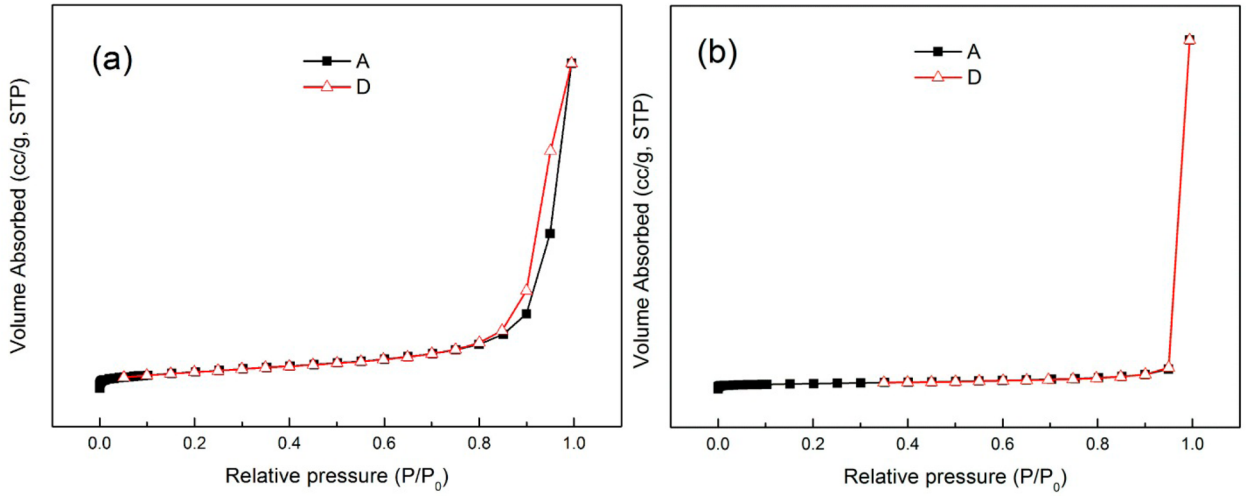

Figure 4. N_2 adsorption−desorption isotherms of (a) DBD-WO_3 and (b) C-WO_3.

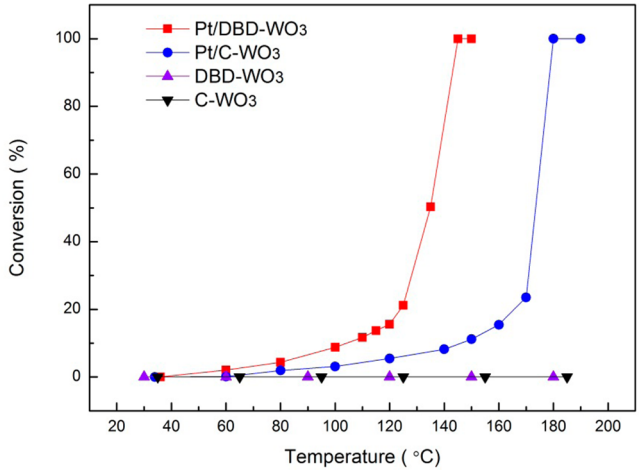

Figure 5. Variation of CO conversion with temperature.

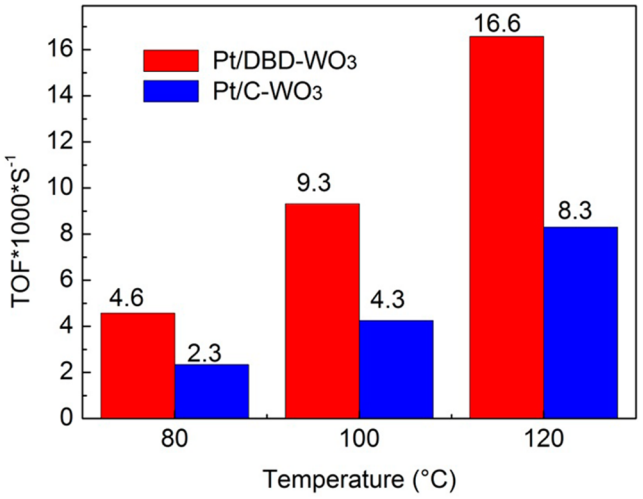

Figure 6. TOF values at 80, 100, and 120 °C for different catalysts.

oxidized samples (DBD-WO_3 and C-WO_3) show higher intensities and are sharper than the peaks of the reduced samples. The peaks at 26−30°disappear after reduction. Meanwhile, the color of the samples changes to dark blue after reduction, which confirms the reduction of the samples.

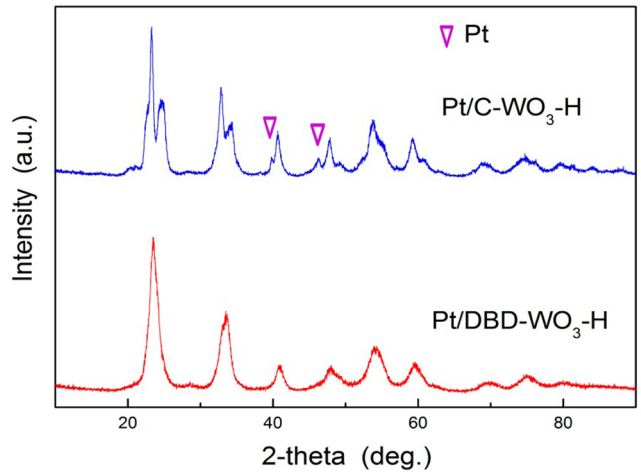

Figure 7. XRD patterns of Pt/DBD-WO_3−H and Pt/C-WO_3−H catalysts.

The DBD-WO_3 was reduced to $H_{0.23}WO_3$ (JCPDS card no. 42-1260), which is similar to a reported work,[31] while C-WO_3 was reduced to $WO_{2.90}$ (JCPDS card no. 36-0102). The difference between the supports after reduction might be due to the different morphologies of the WO_3 materials. From Figure 3, it is clear that DBD-WO_3 exposes more (002) planes and shows a higher specific surface than C-WO_3. Wang et al. reported that H adsorbs preferentially on the under-coordinated O_t site (in the [001] direction) of the surface and migrates into the WO_3, which leads to the formation of surface hydroxyl and H_xWO_3 of Pt/DBD-WO_3−H.[32]

3.2.3. TEM Analyses. Figure 8 shows TEM images of Pt/DBD-WO_3−H and Pt/C-WO_3−H. We can see in these images that the Pt particles are highly dispersed on tungsten oxides. The morphologies of the Pt particles are spherical or hemispherical. The Pt particles over Pt/DBD-WO_3−H are remarkably smaller than those over Pt/C-WO_3−H. We surveyed more than 120 particles and calculated the particle size and the standard deviation of Pt/DBD-WO_3−H and Pt/C-WO_3−H. The average diameters of the Pt particles are 2.1 ± 0.5 and 3.1 ± 1.1 nm, respectively (Figure 8, panels c1 and c2). When we consider the same condition of impregnation and calcination, these results indicate that the support has a

dx.doi.org/10.1021/am502807b | ACS Appl. Mater. Interfaces 2014, 6, 12860−12867

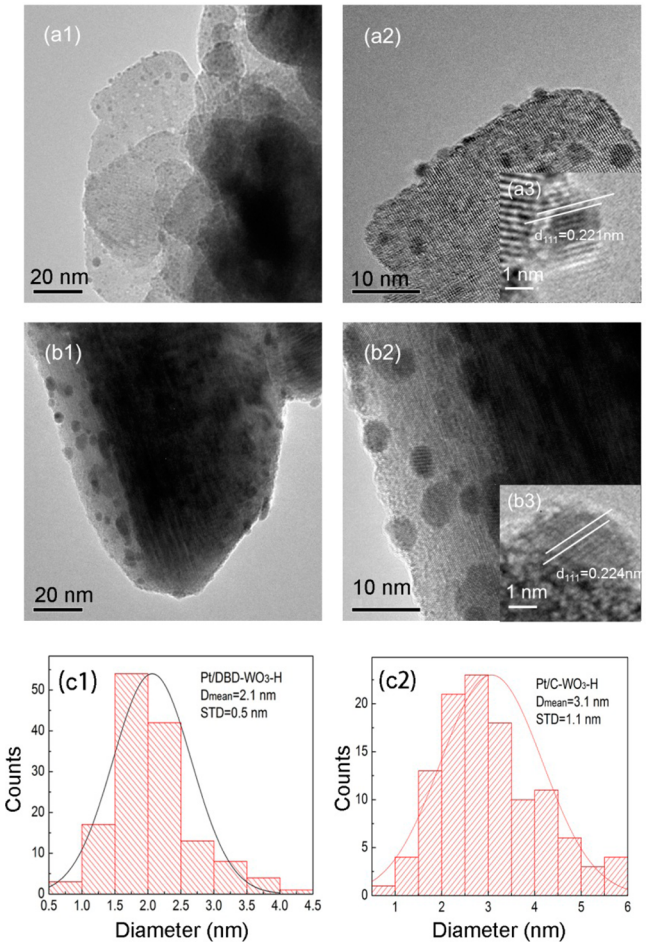

Figure 8. TEM images of (a1−a3) Pt/DBD-WO_3−H and (b1−b3) Pt/C-WO_3−H and (c1 and c2) the corresponding particle size distributions.

significant effect on the size and distribution of Pt particles. The higher specific surface area and the nanolamella morphology of DBD-WO_3 increase the adsorption sites of the support, leading to less sintering and higher dispersion of the Pt particles.

Figure 8a2,a3,b2,b3 shows further structural analysis of the Pt particles. The lattice fringes with d = 0.224 nm are attributed to the Pt (111) (JCPDS card no. 65-2868, d = 2.27 Å). It confirms the crystalline characteristic of Pt particles. Meanwhile, a thin layer of tungsten oxide that partially covers the Pt nanoparticles is observed. This result is in agreement with previous reports.[33,34] It may lead to a change in the properties of noble metal and the support.

3.2.4. H_2-TPR Studies. H_2-TPR profiles of the Pt/DBD-WO_3 and Pt/C-WO_3 catalysts are shown in Figure 9. The Pt/C-WO_3 catalyst exhibits four hydrogen consumption areas with a low-temperature (LT) reduction peak at 185 °C, a middle-temperature (MT) peak at 450 °C, a high-temperature (HT) peak at 800 °C, and a reduction tail up to 900 °C, at which the experiment was terminated. Similar results were obtained from Pt/DBD-WO_3. The LT peak of Pt/DBD-WO_3 shifts to a higher temperature (190 °C), but the MT and HT peaks shift to lower temperatures (400 and 750 °C, respectively).

The LT peaks of the two samples can be attributed to the reduction of Pt ions. The MT and HT peaks are assigned to the reduction of the support. To our knowledge, the reduction of bulk WO_3 usually begins at temperatures higher than 600 °C.[35]

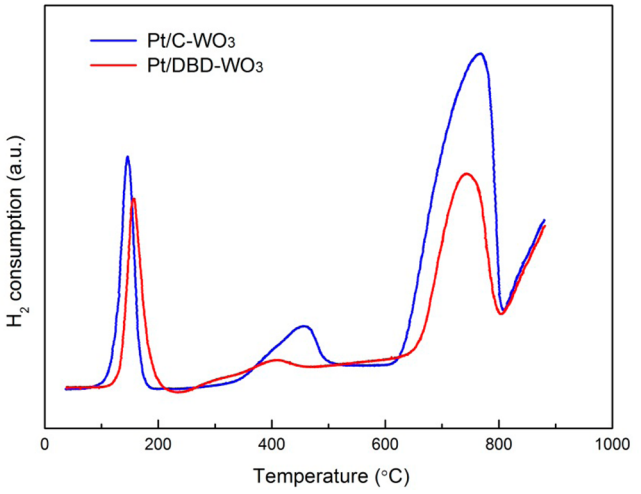

Figure 9. H_2-TPR profiles of (red line) Pt/DBD-WO_3 and (blue line) Pt/C-WO_3.

It can be accelerated with spillover effect.[36] By comparing the two samples, the reduction temperature of DBD-WO_3 shifts to a relatively lower temperature. Furthermore, the higher reduction temperature of Pt on DBD-WO_3 means a stronger interaction between the metal and the support.

3.2.5. XPS Analyses. Figure 10 presents the XPS spectra of Pt 4f over Pt/DBD-WO_3−H and Pt/C-WO_3−H. In the case of

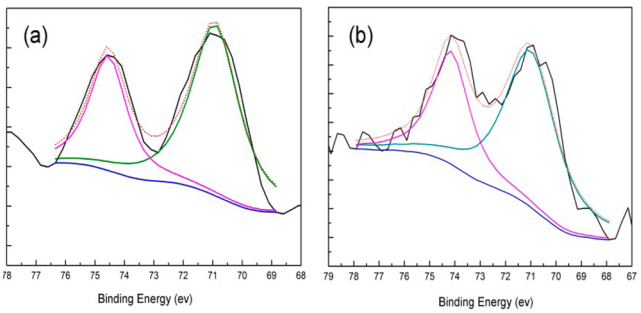

Figure 10. XPS spectra (Pt 4f) of (a) Pt/DBD-WO_3−H and (b) Pt/C-WO_3−H.

Pt/DBD-WO_3−H, two peaks at 70.8 and 74.3 eV, corresponding to Pt $4f_{7/2}$ and Pt $4f_{5/2}$, respectively, are assigned to the binding energies (BE) of Pt^0.[36,37] It confirms that Pt ions are completely reduced under hydrogen thermal treatment, in accordance with XRD. Meanwhile, a slight asymmetry in the signal is observed. For Pt/C-WO_3−H, the peaks of Pt $4f_{7/2}$ and Pt $4f_{5/2}$ shift to 71.0 and 74.2 eV, respectively. When we compare spectra of the two samples, we see that the Pt $4f_{7/2}$ peak of Pt/DBD-WO_3−H shifts to a lower value by approximately 0.2 eV with a slight change in full width at half-maximum (fwhm), which suggests a change in the electronic environment of Pt and a local increase of the electron density on Pt.[37]

The XPS spectra of W 4f are shown in Figure 11. In accordance with other reports,[37,38] the peaks of W 4f in Figure 11a both shift to lower binding energies compared with pure WO_3. After curve fitting is performed, the spectra of W 4f are divided into two pairs of peaks (33.6 and 36.1 eV, attributed to W^{5+}; 35.0 and 37.2 eV, attributed to W^{6+}), confirming the partial reduction of the support. A similar result is shown in

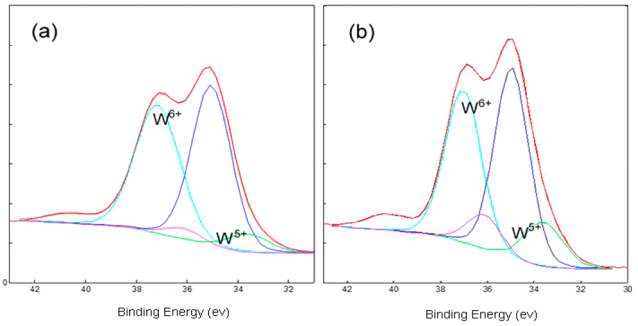

Figure 11. XPS spectra (W 4f) of (a) Pt/DBD-WO_3−H and (b) Pt/C-WO_3−H.

Figure 11b. Therefore, oxygen vacancies of WO_x are formed, and they might have an effect on the catalytic activity.

Figure 12 presents the XPS spectra of O 1s over Pt/DBD-WO_3−H and Pt/C-WO_3−H. Three components at 529.8, 530.5, and 531.5 eV are obtained after curve fitting (Figure 12a). The peak at 530.5 eV can be attributed to the oxygen bonded to W^{6+} (i.e., WO_3).[37] The signal at 531.5 eV is assigned to the surface hydroxyl groups on the sample, which leads to the formation of "tungsten bronze".[38,39] The third peak at 529.8 eV, which is lower than that of WO_3, can be assigned to the atomically adsorbed oxygen on Pt(111).[40,41] However, in the case of Pt/C-WO_3−H, the peak assigned to hydroxyl groups disappears and a new peak at 532.7 eV appears, because of the presence of nonstoichiometric tungsten oxides.[37] The results from O 1s spectra are in accordance with the XRD results.

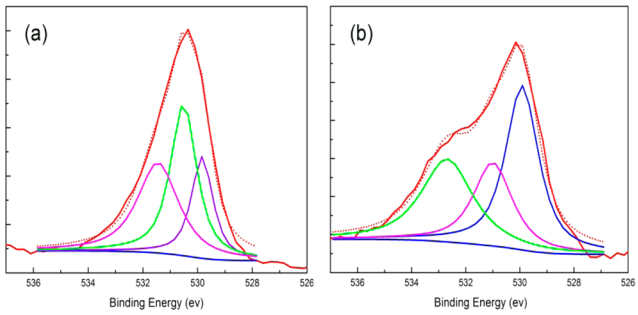

Figure 12. XPS spectra (O 1s) of (a) Pt/DBD-WO_3−H and (b) Pt/C-WO_3−H.

The results above demonstrate a strong metal−support interaction (SMSI). It suggests that a reduction of WO_3 occurs in the presence of Pt at 300 °C, which is in accordance with XRD and TPR. Meanwhile, a lower BE and a higher electron density of Pt on DBD-WO_3 are observed. When we consider the same reduction conditions, the interaction between Pt and support of Pt/DBD-WO_3−H should be stronger than that of Pt/C-WO_3−H with more electron transfer from support to Pt. The surface atomic ratios are presented in Table 2. No chlorine content is detected, indicating the complete removal of chlorine ions. The Pt/W atomic ratio of Pt/C-WO_3−H is 0.113, while it is 0.022 over Pt/DBD-WO_3−H, much lower than the former. It is similar to other reports with Pt/TiO_2, which exhibits the SMSI effect.[42,43] Briefly, the decrease of Pt/W can be attributed to a strong interaction between Pt and the support. Hydrogen atoms chemisorbed on Pt can interact with oxygen atoms from the support located at the metal−support interface to form surface hydroxyls or oxygen vacancies and partially reduce W^{5+}.[44] Meanwhile, the metal particles are decorated with the migration of WO_x fragments, leading to the decrease of exposed metal surfaces, which is in accordance with the TEM results. This decoration would significantly promote the metal−support interaction, and electrons can transfer from support to Pt, leading to the increase of electron density of Pt atoms. In addition, Zheng et al. reported that surface OH groups on TiO_2 surfaces facilitate adsorption and activation of O_2 molecules, which directly contributes to the supply of active oxygen species during CO oxidation.[45] Therefore, it is likely that the surface OH groups on Pt/DBD-WO_3 provide a similar promotion of activity.

3.2.6. DRIFT Studies. Figure 13 shows the DRIFT spectra of CO adsorbed on Pt/DBD-WO_3−H and Pt/C-WO_3−H at 25 °C. A series of bands ranging from 2050−2200 cm^{-1} are observed on the two samples (Figure 13). The band located at ~2180 cm^{-1} might be assigned to the CO adsorbed on weak Lewis acid sites of the support, namely, W^{6+}-CO, which is similar to the results of other reports.[46,47] The bands at ~2120 and ~2165 cm^{-1} are attributed to gaseous CO (supported by the spectra of DBD-WO_3 and C-WO_3). The bands located at ~2115 cm^{-1} are attributed to the CO adsorbed either on the reduced WO_3, namely, W^{5+}-CO, or on the Pt^{2+}. When we consider the XPS results and the lower intensity compared with that of W^{6+}-CO, the bands are attributed to W^{5+}-CO.[46] The

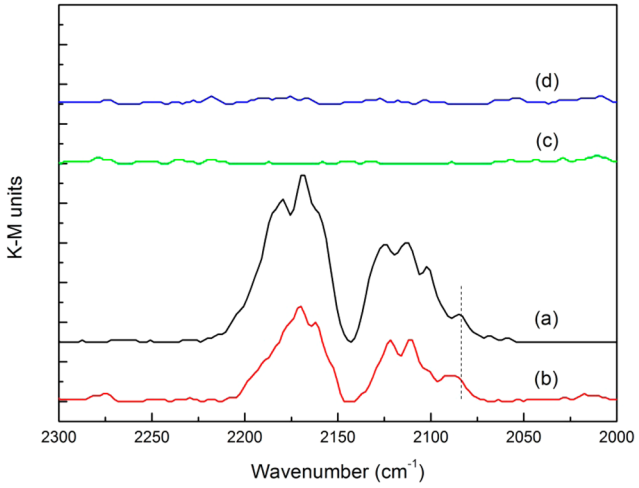

Figure 13. DRIFT spectra of (a) Pt/DBD-WO_3−H and (b) Pt/C-WO_3−H exposed to CO for 30 min at 25 °C and spectra of (c) Pt/DBD-WO_3−H and (d) Pt/C-WO_3−H purged with argon for 1 min.

Table 2. Binding Energies (BE) of Core Electrons and Surface Atomic Ratio of Two Catalysts

		W $4f_{7/2}$ BE (eV)					
sample	Pt $4f_{7/2}$ BE (eV)	W^{5+}	W^{6+}	O 1s BE (eV)			atomic ratio (Pt/W)
Pt/DBD-WO_3−H	70.8	33.6	35.0	529.8	530.5	531.5	0.022
Pt/C-WO_3−H	71.0	33.6	34.9	529.9	531.0	532.7	0.113

bands at ~2100 cm^{-1} should be assigned to the C−O stretching mode of the O-bonded CO.[48] The bands at ~2085 cm^{-1} are assigned to CO terminally adsorbed on Pt,[49] while the bands at ~1850 cm^{-1} assigned to the bridging CO adsorbed on Pt are not evident. This indicates a lack of bridging CO.[49] When the two samples are compared, the band assigned to the Pt-CO in Pt/DBD-WO_3−H shifts to a lower wavenumber by approximately 5 cm^{-1}. On the basis of Blyholder's model, an increase of the electron density of Pt promotes the back-donation of electrons of the metal into the CO $2\pi^*$ antibonding orbitals, leading to a decrease of the v(CO) frequency.[50] This result is in accordance with XPS results. Moreover, for Pt/DBD-WO_3−H, it is clear that the relative intensities of the bands at 2179 and 2102 cm^{-1} are distinctly higher than those of Pt/C-WO_3−H. This result should be attributed to the higher specific surface area of DBD-WO_3. In Figure 13, lines c and d show the DRIFT spectra of CO adsorbed on Pt/DBD-WO_3−H and Pt/C-WO_3−H purged with Ar for 3 min at ambient temperature. All the bands observed in Figure 13 disappear rapidly by Ar purge, indicating a weak adsorption of CO on the catalysts and complete desorption at a low temperature. These results are in agreement with other report on Pt/TiO_2 catalysts and demonstrate that an increase in the electron density of Pt would alter its chemisorption properties and weaken the Pt-CO bonding.[42] This definitely promotes the activity and inhibits catalyst poisoning. Consequently, the Pt/DBD-WO_3 shows better activity for CO oxidation.

4. CONCLUSIONS

WO_3 is a very important functional material with many promising applications. In this work, WO_3 has been applied as the supporting material of Pt catalyst for CO oxidation. By comparing WO_3 nanolamella supported Pt catalyst with WO_3 nanoparticle supported one, we confirm that the morphology of WO_3 has a significant influence on the activity of Pt catalysts for CO oxidation. The catalyst characterization shows that WO_3 nanolamella supported Pt catalyst possesses higher Pt dispersion, improved metal−support interaction with a higher electron density of Pt, and a weak adsorption of CO, leading to the significantly enhanced activity for CO oxidation.

However, we reported here a rapid, easy, and convenient way to generate WO_3 nanolamella by the novel dielectric-barrier discharge plasma decomposition with air as the plasma generating gas. Such production is operated at atmospheric pressure and low temperature. It does not need any extra chemicals, and thus, it is a green method. Considering the extensive applications of WO_3 and Pt catalysts, the present study is leading to many other important applications that will be reported in our future works.

■ ASSOCIATED CONTENT

Supporting Information

BJH pore size distribution and TEM images of the used catalysts. This material is available free of charge via the Internet at http://pubs.acs.org.

■ AUTHOR INFORMATION

Corresponding Author

*E-mail: ughg_cjl@yahoo.com. Fax: +86 22 27406490.

Author Contributions

The manuscript was written through contributions of all authors. All authors have given approval to the final version of the manuscript

Notes

The authors declare no competing financial interest.

■ ACKNOWLEDGMENTS

This work was supported by the National Natural Science Foundation of China (Grant No. 91334206).

■ REFERENCES

(1) Anastas, P. T.; Kirchhoff, M. M.; Williamson, T. C. Catalysis as a Foundational Pillar of Green Chemistry. *Appl. Catal., A* **2001**, *221*, 3−13.

(2) Varade, D.; Abe, H.; Yamauchi, Y.; Haraguchi, K. Superior CO Catalytic Oxidation on Novel Pt/Clay Nanocomposites. *ACS Appl. Mater. Interfaces* **2013**, *5*, 11613−11617.

(3) Kim, S. K.; Kim, C.; Lee, J. H.; Kim, J.; Lee, H.; Moon, S. H. Performance of Shape-Controlled Pd Nanoparticles in the Selective Hydrogenation of Acetylene. *J. Catal.* **2013**, *306*, 146−154.

(4) Chen, G.; Zhou, Y.; Long, Z. Y.; Wang, X. C.; Li, J.; Wang, J. Mesoporous Polyoxometalate-Based Ionic Hybrid As a Triphasic Catalyst for Oxidation of Benzyl Alcohol with H_2O_2 on Water. *ACS Appl. Mater. Interfaces* **2014**, *6*, 4438−4446.

(5) Zhou, T.; Jang, K.; Jang, B. W. L. Ionic Liquid and Plasma Effects on SiO_2 Supported Pd for Selective Hydrogenation of Acetylene. *Catal. Today* **2013**, *211*, 147−155.

(6) Huang, M. H.; Rej, S.; Hsu, S. C. Facet-Dependent Properties of Polyhedral Nanocrystals. *Chem. Commun.* **2014**, *50*, 1634−1644.

(7) Hu, B. X.; Frueh, S.; Garces, H. F.; Zhang, L. C.; Aindow, M.; Brooks, C.; Kreidler, E.; Suib, S. L. Selective Hydrogenation of CO_2 and CO to Useful Light Olefins over Octahedral Molecular Sieve Manganese Oxide Supported Iron Catalysts. *Appl. Catal., B* **2013**, *132*, 54−61.

(8) Li, W. Z.; Kovarik, L.; Mei, D. H.; Liu, J.; Wang, Y.; Peden, C. H. F. Stable Platinum Nanoparticles on Specific $MgAl_2O_4$ Spinel Facets at High Temperatures in Oxidizing Atmospheres. *Nat. Commun.* **2014**, *4*, 2481.

(9) Wei, Z. H.; Sun, J. M.; Li, Y.; Datye, A. K.; Wang, Y. Bimetallic Catalysts for Hydrogen Generation. *Chem. Soc. Rev.* **2012**, *41*, 7994−8008.

(10) Zhang, S. R.; Nguyen, L.; Zhu, Y.; Zhan, S. H.; Tsung, C. K.; Tao, F. In-Situ Studies of Nanocatalysis. *Acc. Chem. Res.* **2013**, *46*, 1731−1739.

(11) Wang, L.; Zhang, S. R.; Zhu, Y.; Patlolla, A.; Shan, J. J.; Yoshida, H.; Takeda, S.; Frenkel, A. I.; Tao, F. Catalysis and In Situ Studies of Rh_1/Co_3O_4 Nanorods in Reduction of NO with H_2. *ACS Catal.* **2013**, *3*, 1011−1019.

(12) Hu, Y. H. Solid-Solution Catalysts for CO_2 Reforming of Methane. *Catal. Today* **2009**, *148*, 206−211.

(13) Torrente-Murciano, L.; Gilbank, A.; Puertolas, B.; Garcia, T.; Solsona, B.; Chadwick, D. Shape-Dependency Activity of Nano-structured CeO_2 in the Total Oxidation of Polycyclic Aromatic Hydrocarbons. *Appl. Catal., B* **2013**, *132*, 116−122.

(14) Wang, H. P.; Liu, C. J. Preparation and Characterization of SBA-15 Supported Pd Catalyst for CO Oxidation. *Appl. Catal., B* **2011**, *106*, 672−680.

(15) Koo, K. Y.; Jung, U. H.; Yoon, W. L. A Highly Dispersed Pt/γ-Al_2O_3 Catalyst Prepared via Deposition−Precipitation Method for Preferential CO Oxidation. *Int. J. Hydrogen Energy* **2014**, *39*, 5696−5703.

(16) Li, N.; Chen, Q. Y.; Luo, L. F.; Huang, W. X.; Luo, M. F.; Hu, G. S.; Lu, J. Q. Kinetic Study and the Effect of Particle Size on Low Temperature CO Oxidation over Pt/TiO_2 Catalysts. *Appl. Catal., B* **2013**, *142*, 523−532.

(17) An, K.; Alayoglu, S.; Musselwhite, N.; Plamthottam, S.; Melaet, G.; Lindeman, A. E.; Somorjai, G. A. Enhanced CO Oxidation Rates at the Interface of Mesoporous Oxides and Pt Nanoparticles. *J. Am. Chem. Soc.* **2013**, *135*, 16689−16696.
(18) Kida, T.; Nishiyama, A.; Hua, Z. Q.; Suematsu, K.; Yuasa, M.; Shimanoe, K. WO_3 Nanolamella Gas Sensor: Porosity Control Using SnO_2 Nanoparticles for Enhanced NO_2 Sensing. *Langmuir* **2014**, *30*, 2571−2579.
(19) Arai, T.; Horiguchi, M.; Yanagida, M.; Gunji, T.; Sugihara, H.; Sayama, K. Complete Oxidation of Acetaldehyde and Toluene over a Pd/WO_3 Photocatalyst under Fluorescent- or Visible-Light Irradiation. *Chem. Commun.* **2008**, 5565−5567.
(20) Amano, F.; Li, D.; Ohtani, B. Fabrication and Photoelectrochemical Property of Tungsten(VI) Oxide Films with a Flake-Wall Structure. *Chem. Commun.* **2010**, *46*, 2769−2771.
(21) Wang, J.; Khoo, E.; Lee, P. S.; Ma, J. Synthesis, Assembly, and Electrochromic Properties of Uniform Crystalline WO_3 Nanorods. *J. Phys. Chem. C* **2008**, *112*, 14306−14312.
(22) Ulgen, A.; Hoelderich, W. Conversion of Glycerol to Acrolein in the Presence of WO_3/ZrO_2 Catalysts. *Catal. Lett.* **2009**, *131*, 122−128.
(23) Ciardellia, C.; Novaa, I.; Tronconi, E.; Chatterjeeb, D.; Bandl-Konradb, B. A "Nitrate Route" for the Low Temperature "Fast SCR" Reaction over a V_2O_5-WO_3/TiO_2 Commercial Catalyst. *Chem. Commun.* **2004**, 2718−2719.
(24) Pan, Y. X.; Kuai, P. Y.; Liu, Y.; Ge, Q. F.; Liu, C. J. Promotion Effects of Ga_2O_3 on CO_2 Adsorption and Conversion over a SiO_2-Supported Ni Catalyst. *Energy Environ. Sci.* **2010**, *3*, 1322−1325.
(25) Zhao, B. R.; Yan, X. L.; Zhou, Y.; Liu, C. J. Effect of Catalyst Structure on Growth and Reactivity of Carbon Nanofibers over Ni/$MgAl_2O_4$. *Ind. Eng. Chem. Res.* **2013**, *52*, 8182−8188.
(26) Yan, X. L.; Liu, Y.; Zhao, B. R.; Wang, Y.; Liu, C. J. Enhanced Sulfur Resistance of Ni/SiO_2 Catalyst for Methanation via the Plasma Decomposition of Nickel Precursor. *Phys. Chem. Chem. Phys.* **2013**, *15*, 12132−12138.
(27) Yan, X. L.; Liu, Y.; Zhao, B. R.; Wang, Z.; Wang, Y.; Liu, C. J. Methanation over Ni/SiO_2: Effect of The Catalyst Preparation Methodologies. *Int. J. Hydrogen Energy* **2013**, *38*, 2283−2291.
(28) Liu, Y.; Pan, Y. X.; Wang, Z. J.; Kuai, P. Y.; Liu, C. J. Facile and Fast Template Removal from Mesoporous MCM-41 Molecular Sieve using Dielectric-Barrier Discharge Plasma. *Catal. Commun.* **2010**, *11*, 551−554.
(29) Ye, J. Y.; Liu, C. J. $Cu_3(BTC)_2$: CO Oxidation over MOF Based Catalysts. *Chem. Commun.* **2011**, *47*, 2167−2169.
(30) Xie, Y. P.; Liu, G.; Yin, L. C.; Cheng, H. M. Crystal Facet-Dependent Photocatalytic Oxidation and Reduction Reactivity of Monoclinic WO_3 for Solar Energy Conversion. *J. Mater. Chem.* **2012**, *22*, 6746−6751.
(31) Chen, H. J.; Xu, N. S.; Deng, S. Z.; Lu, D. Y.; Li, Z. L.; Zhou, J.; Chen, J. Gasochromic Effect and Relative Mechanism of WO_3 Nanowire Films. *Nanotechnology* **2007**, *18*, 205701.
(32) Wang, F. G.; Valentin, C. D.; Pacchioni, G. DFT Study of Hydrogen Adsorption on the Monoclinic WO_3 (001) Surface. *J. Phys. Chem. C* **2012**, *116*, 10672−10679.
(33) Micoud, F.; Maillard, F.; Bonnefont, A.; Job, N.; Chatenet, M. The Role of the Support in CO_{ads} Monolayer Electrooxidation on Pt Nanoparticles: Pt/WO_x vs. Pt/C. *Phys. Chem. Chem. Phys.* **2010**, *12*, 1182−1193.
(34) Regalbuto, J. R.; Fleisch, T. H.; Wolf, E. E. An Integrated Study of $Pt/WO_3/SiO_2$ catalysts for the NO-CO reaction: I. Catalyst Characterization by XRD, Chemisorption, and XPS. *J. Catal.* **1987**, *107*, 114−128.
(35) Sica, A. M.; Gigola, C. E. Interaction of CO, NO. and NO/CO over Pd/γ-Al_2O_3 and Pd-WO_x/γ-Al_2O_3 Catalysts. *Appl. Catal., A* **2003**, *239*, 121−139.
(36) Alonso, F.; Riente, P.; Rodríguez-Reinoso, F.; Ruiz-Martinez, J.; Sepúlveda-Escribano, A.; Yus, M. Platinum Nanoparticles Supported on Titania As an Efficient Hydrogen-Transfer Catalyst. *J. Catal.* **2008**, *260*, 113−118.
(37) Lewera, A.; Timperman, L.; Roguska, A.; Alonso-Vante, N. Metal-Support Interactions between Nanosized Pt and Metal Oxides (WO_3 and TiO_2) Studied Using X-ray Photoelectron Spectroscopy. *J. Phys. Chem. C* **2011**, *115*, 20153−20159.
(38) Fleisch, T. H.; Mains, G. J.; An, X. P. S. Study of the UV Reduction and Photochromism of MoO_3 and WO_3. *J. Chem. Phys.* **1982**, *76*, 780−786.
(39) Shim, H. S.; Kim, J. W.; Sung, Y. E.; Kim, W. B. Electrochromic Properties of Tungsten Oxide Nanowires Fabricated by Electrospinning Method. *Sol. Energy Mater. Sol. Cells* **2009**, *93*, 2062−2068.
(40) Fisher, G. B.; Gland, J. L. The Interaction of Water with the Pt(111) Surface. *Surf. Sci.* **1980**, *94*, 446−455.
(41) Parkinson, C. R.; Walker, M.; McConville, C. F. Reaction of Atomic Oxygen with a Pt(111) Surface: Chemical and Structural Determination Using XPS, CAICISS, and LEED. *Surf. Sci.* **2003**, *545*, 19−33.
(42) Alexeev, O. S.; Chin, S. Y.; Engelhard, M. H.; Ortiz-Soto, L.; Amiridis, M. D. Effects of Reduction Temperature and Metal−Support Interactions on the Catalytic Activity of Pt/γ-Al_2O_3 and Pt/TiO_2 for the Oxidation of CO in the Presence and Absence of H_2. *J. Phys. Chem. B* **2005**, *109*, 23430−23443.
(43) Pesty, F.; Steinrück, H. P.; Madey, T. E. Thermal Stability of Pt Films on TiO_2(110): Evidence for Encapsulation. *Surf. Sci.* **1995**, *339*, 83−95.
(44) Baker, R. T. K.; Prestridge, E. B.; Garten, R. L. Electron Microscopy of Supported Metal Particles II. Further Studies of Pt/TiO_2. *J. Catal.* **1979**, *59*, 293−302.
(45) Zheng, Z. F.; Teo, J.; Chen, X.; Liu, H. W.; Yuan, Y.; Waclawik, E. R.; Zhong, Z. Y.; Zhu, H. Y. Correlation of the Catalytic Activity for Oxidation Taking Place on Various TiO_2 Surfaces with Surface OH Groups and Surface Oxygen Vacancies. *Chem.—Eur. J.* **2010**, *16*, 1202−1211.
(46) Panagiotopoulou, P.; Christodoulakis, A.; Kondarides, D. I.; Boghosian, S. Particle Size Effects on the Reducibility of Titanium Dioxide and Its Relation to the Water−Gas Shift Activity of Pt/Ti_2 Catalysts. *J. Catal.* **2006**, *240*, 114−125.
(47) Hadjiivanov, K.; Lamotte, J.; Lavalley, J. C. FTIR Study of Low-Temperature CO Adsorption on Pure and Ammonia-Precovered TiO_2 (Anatase). *Langmuir* **1997**, *13*, 3374−3381.
(48) Areán, C. O.; Manoilova, O. V.; Delgado, M. R.; Tsyganenko, A. A.; Garrone, E. Formation of Several Types of Coordination Complexes upon CO Adsorption on the Zeolite Li-ZSM-5. *Phys. Chem. Chem. Phys.* **2001**, *3*, 4187−4188.
(49) Moses-DeBusk, M.; Yoon, M.; Allard, L. F.; Mullins, D. R.; Wu, Z. L.; Yang, X. F.; Veith, G.; Stocks, G. M.; Narula, C. K. CO Oxidation on Supported Single Pt Atoms: Experimental and ab Initio Density Functional Studies of CO Interaction with Pt Atom on θ-Al_2O_3(010) Surface. *J. Am. Chem. Soc.* **2013**, *135*, 12634−12645.
(50) Blyholder, G. Molecular Orbital View of Chemisorbed Carbon Monoxide. *J. Phys. Chem.* **1964**, *68*, 2772−2777.